Journal of Environmental Chemical Engineering 9 (2021) 105589

Contents lists available at ScienceDirect

Journal of Environmental Chemical Engineering

journal homepage: www.elsevier.com/locate/jece

Mesoporous Fe-doped MgO nanoparticles as a heterogeneous photo-Fenton-like catalyst for degradation of salicylic acid in wastewater

Manoj Silva [a,1], John Baltrus [b,2], Clinton Williams [c,3], Allan Knopf [c], Lihua Zhang [d], Jonas Baltrusaitis [a,*,4]

[a] Department of Chemical and Biomolecular Engineering, Lehigh University, B336 Iacocca Hall, 111 Research Drive, Bethlehem, PA 18015, USA
[b] National Energy Technology Laboratory, US Department of Energy, 626 Cochrans Mill Road, Pittsburgh, PA 15236, USA
[c] USDA-ARS, US Arid Land Agricultural Research Center, 21881 N. Cardon Ln, Maricopa, AZ 85138, USA
[d] Brookhaven National Laboratory, Center for Functional Nanomaterials, Upton, NY 11973, USA

ARTICLE INFO

Editor: Dr. G. Palmisano

Keywords:
Heterogeneous photo-Fenton
Catalysis
MgO nanoparticles
Wastewater treatment
Mesoporous catalysts

ABSTRACT

Mesoporous Fe-doped MgO nanoparticles were synthesized using a facile sol-gel method and utilized for photo-Fenton-like degradation of salicylic acid (SA). The MgO surface dissolution facilitated an increase in the pH under the reaction conditions that allowed the Fe-MgO catalyst to be active without detectable iron leaching. Under simulated solar radiation, SA was completely degraded with an initial rate constant of 0.048 min^{-1} at the optimal reaction conditions of 500 ppm loading of 5% Fe-MgO, 20 mM H_2O_2 concentration, and 50 ppm SA concentration. The catalyst was stable over 5 reaction cycles. The Fe-MgO catalyst was shown to have a surface area up to 171 m^2/g and contain hematite (Fe_2O_3) nanoparticles with octahedrally coordinated iron catalytic centers, as inferred from diffuse reflectance UV–vis measurements. Post-reaction catalyst characterization showed that some Fe^{2+} was present in the catalyst due to the redox cycle during the chain initiation and propagation steps of the reaction.

1. Introduction

Water scarcity combined with its pollution by toxic contaminants is one of the key challenges facing humanity [1]. An increasing population has led to a rise in urbanization, industrialization, as well as growth in high intensity agriculture, which has led to generation of diverse wastewater streams containing various contaminants and pathogens that are eventually discharged into watersheds [2–4]. Pharmaceuticals and personal care products (PPCPs) have been identified as an emerging contaminant due to their presence in wastewater, surface water, and groundwater [5–8]. In particular, anti-inflammatory agents and analgesics, antibiotics, β-blockers, antihistamines, and antidepressants are some of the most commonly detected PPCPs in wastewater streams [6,7]. Traditionally, biological degradation methods have been used to treat the organic matter in wastewater [9,10]. However, recalcitrant organic compounds are highly resistant to biological degradation and thus, require further treatment methods [11]. Advanced oxidation processes (AOPs) have been demonstrated to be highly active toward removing such recalcitrant organic contaminants [12,13]. Studies have shown that environmental discharge water can be treated using these techniques and then added to the drinking water supply without risk to human health [12,14].

AOPs are of particular interest since they allow for the degradation of organic contaminants that are otherwise recalcitrant and ubiquitous in municipal, industrial, and agricultural wastewater [15]. The Fenton reaction is an AOP that utilizes iron and H_2O_2, which are two environmentally benign compounds that are safe to handle. The Fenton reaction uses $Fe^{2+}_{(aq)}$ ions to produce reactive oxygen species (ROS) from H_2O_2. The chain initiation step for the Fenton reaction occurs rapidly with Fe^{2+} as shown in (1) but many heterogeneous catalysts are synthesized with Fe^{3+} which has a significantly smaller rate constant than the Fe^{2+} species for this step as shown in (2) [15].

* Corresponding author.
E-mail address: job314@lehigh.edu (J. Baltrusaitis).
[1] 0000-0002-5353-006X
[2] 0000-0003-3253-9193
[3] 0000-0002-2554-5061
[4] 0000-0001-5634-955X

https://doi.org/10.1016/j.jece.2021.105589
Received 18 March 2021; Received in revised form 17 April 2021; Accepted 25 April 2021
Available online 1 May 2021

$$Fe^{2+} + H_2O_2 \rightarrow Fe^{3+} + HO^{\bullet} + OH^{-} \qquad k = 40\text{–}80 M^{-1}s^{-1} \quad (1)$$

$$Fe^{3+} + H_2O_2 \rightarrow Fe^{3+} + HO_2^{\bullet} + H^{+} \qquad k = 0.001\text{–}0.01\ M^{-1}s^{-1} \quad (2)$$

Therefore, a light source is used to photo-reduce the Fe^{3+} to Fe^{2+}. This process is referred to as a photo-Fenton-like degradation, where a light source with a wavelength similar to the ligand-to-metal charge transfer (LMCT) wavelength of the catalyst is used to transfer an electron and reduce the Fe^{3+} [16]. This photo-reduction initiates the faster chain initiation step, generating sufficient ROS to start the degradation process. While the homogeneous Fenton reaction is highly effective, it intrinsically faces two challenges that prevent successful large-scale implementation including (a) the solution pH of ~3 and (b) the waste iron sludge generated. Therefore, research has focused on heterogeneous Fenton catalysts due to their easier separation and reusability, as well as a solution pH closer to the circumneutral which can be discharged into the watershed [15,17,18].

Fe-based heterogeneous catalysts have been extensively studied for the photo-Fenton-like reaction with a number of reports focusing on bulk minerals such as hematite, goethite and magnetite, as well as supported catalysts [15,17–19]. Bulk minerals possess low surface area and thus, research has focused on using porous supports with higher surface area in order to achieve faster kinetics with better active site dispersion, lower use of Fe precursor, and improve diffusion through the catalyst particle [13]. A variety of supports have been studied including SiO_2, Al_2O_3, as well as various clay materials in order to improve the catalytic performance [13,15,19–22]. Such catalysts have led to complete oxidation of target molecules with fast kinetics, and typically the supports remain inert during the reaction [15,23].

AOP design based on a photo-Fenton-like process requires evaluation of process parameters such as catalyst loading, H_2O_2 concentration, light source, contaminant concentration, and pH. Among these parameters, the pH of the solution plays an important role since low pH conditions lead to iron leaching out and performing the homogeneous Fenton reaction, which is undesirable for a heterogeneous catalyst [24]. Therefore, higher pH conditions are preferred to prevent the dissolution of Fe from the catalyst. Given the legal Fe limit in wastewater set by the European Community Directives is 2 ppm, operating at a basic pH regime is beneficial to ensure the catalyst does not leach Fe into the effluent [18,25]. Typically, such pH control is achieved using buffers or titration, which increases operational costs [26,27]. To circumvent this issue, producing a catalyst that can both catalytically convert H_2O_2 to ROS, and regulate the pH at a basic level would be beneficial.

This study reports mesoporous Fe-doped MgO nanoparticles synthesized via a facile sol-gel method as a photo-Fenton-like catalyst that possesses dual functionality. The Fe sites degrade target organic molecules via ROS generation, and the MgO surface dissolution controls the pH near the catalysts [28] thus preventing dissolution and, potentially, loss of iron into the solution. Mesoporous MgO nanoparticles have previously shown to be excellent adsorbents due to the enhanced intraparticle diffusion properties compared to that of bulk materials [29]. These transport properties can allow for better catalytic activity due to faster intraparticle diffusion. SA was used as a model compound since it is a common ingredient in nonsteroidal anti-inflammatory drugs (NSAIDs) and has been detected at up to 27.8 ppm in North American wastewater treatment plants [5]. This report presents a thorough study of catalyst performance by reporting the effects of varying Fe loadings on the support, catalyst loading in the reaction, H_2O_2 concentration, catalyst reusability, and detailed characterization of the catalyst bulk structure and surface region both before and after the reaction.

2. Experimental methods

2.1. Mesoporous Fe-MgO nanoparticle synthesis

A previously developed facile, sol-gel procedure was modified and used to synthesize 2.5%, 5%, and 10% (by weight) Fe-MgO [29,30]. Briefly, a solution of $Mg(NO_3)_2{\cdot}6H_2O$ (MilliporeSigma, 99%) and iron (III) nitrate nonahydrate (Acros, 98+%) was prepared in methanol with the required mass ratios and a 0.59 M NaOH/methanol solution was added dropwise under reflux temperature. After 30 min of reaction at reflux temperature, the resulting precipitate was collected by centrifugation, washed three times using a 1:1 ratio of ethanol/water solution and dried at 80 °C overnight. The dry solid was calcined at 450 °C for 2 h (2 °C/min ramp rate) in static air. Then, 0.5 g of the prepared catalyst was added to 40 mL deionized water and stirred for 12 h. After stirring, the gel was separated and dried at 80 °C. The sample was then calcined at 450 °C for 2 h (2 °C/min ramp rate) in static air to obtain the final catalyst.

2.2. Catalyst physicochemical characterization methods

2.2.1. Powder X-ray diffraction

The crystal structure of all catalysts was confirmed using powder X-ray diffraction (Empyrean, PANalytical B.V.). The applied current was 40 mA and the applied voltage was 45 kV. The X-ray mirror that was used was a graded, flat Bragg-Brentano HD mirror, with the step size set to 0.0131 degrees.

2.2.2. N_2 physisorption

N_2 physisorption was used to measure surface area using a Micromeritics ASAP2020 surface area and porosimetry system. Samples were degassed at 250 °C before analysis.

2.2.3. Atomic absorption spectroscopy (AAS)

Perkin-Elmer AAnalyst200 AAS was utilized with an air-acetylene flame to measure iron concentrations in aqueous solutions. A 1000 ppm Fe standard solution from PerkinElmer was used to prepare calibration standards.

2.2.4. Mass spectrometry (MS)

A Micromass Quattro Micro API (Micromass UK LTD) was used for mass spectral characterization of the reaction solution. A Waters Alliance HPLC pump, column heater, and autosampler were used for sample injection.

2.2.5. X-ray photoelectron spectroscopy (XPS)

XPS analysis was carried out with a ULVAC-PHI VersaProbe III instrument using a monochromatized Al Kα X-ray source (1486.6 eV). The pass energy of the analyzer was 55.5 eV, the acquisition area had a diameter of 100 μm, and the scan step size was 0.1 eV. Binding energies were corrected for charging by referencing to the C 1s peak at 285.0 eV. Atomic concentrations were calculated from the areas under individual high-resolution XPS spectra using manufacturer-provided sensitivity factors. CasaXPS (www.casaxps.com) was used for spectra manipulation and quantification.

2.2.6. High-angle annular dark-field scanning transmission electron microscopy and energy dispersive X-ray spectroscopy, high-resolution transmission electron microscopy (HAADF-STEM EDS and HR-TEM)

HAADF STEM EDS was used to confirm dopant distribution. A Scanning Transmission Electron Microscope (FEI Talos 200x) equipped with a four-quadrant 0.9-sr spectrometer was used for elemental and compositional mapping. HRTEM imaging was used to study the nanocrystals and was performed on a JEOL2100F operating at 200 kV.

2.2.7. Ultraviolet–visible diffuse reflectance (UV–vis DR)

UV–vis DR spectra were obtained using an Agilent Cary Series 5000 UV–vis–NIR spectrophotometer employing an integration sphere diffuse reflectance attachment (Harrick Praying Mantis Attachment, DRA-2). The sample was loaded as a powder (~20 mg) into an in situ environmental cell (Harrick, HVC-DR2 with a CaF_2 window). Each spectrum

was taken from 200 to 800 nm. MgO was used as a standard for background absorbance, and the edge energies (E_g) were calculated using a Microsoft Excel Macro spreadsheet. All measurements were collected under ambient conditions. The UV–vis spectra were processed with Microsoft Excel software, consisting of calculation of the Kubelka-Munk function, $F(R_\infty)$, which was extracted from the UV–vis DRS absorbance. The edge energy (Eg) for allowed transitions was determined by finding the intercept of the straight line in the low-energy rise of a plot of $[F(R^\infty) h\nu]^{1/n}$, where n = 0.5 for the direct allowed transition, vs hν, where hν is the incident photon energy [31–33].

2.3. Photocatalytic degradation experiments

The SA solution was prepared by dissolving SA (Acros Organics, 99+%) in deionized water (Millipore). A glass vessel containing 100 mL volume of SA solution was used in all experiments. The vessel was then exposed to a 350 W Xenon lamp (Newport), which provided an illumination intensity of approximately 100 mW cm^{-2}. A 1 mL aliquot of solution was periodically filtered with a 0.22 μm membrane and measured immediately with UV–vis to quantify the SA concentration. A calibration curve was generated using a set of SA standard concentrations. The absorbance for the major SA peak at 296 nm at each concentration was fitted to the Beer's law equation to generate a linear calibration. Absorbance measurements were collected using a UV−vis 2600 spectrophotometer equipped with an ISR-2600-Plus integrating sphere attachment (Shimadzu). The rate of SA degradation was defined by the first-order rate equation [34] shown by Eq. (3).

$$C(t) = C_0 e^{-kt} \quad (3)$$

The rate constant k (min^{-1}) in Eq. (3) is the first-order rate constant for the degradation of SA. The initial kinetics were calculated using the 0–15 min time range. The experiments were conducted in triplicate wherever error bars are shown. The quenching experiments were conducted using OH radical scavenger tert-butanol (TBA, Millipore-Sigma) and O_2^- radical scavenger chloroform ($CHCl_3$, Millipore-Sigma).

3. Results and discussion

3.1. Salicylic acid degradation kinetics

To evaluate the photo-Fenton-like performance of the Fe-MgO catalyst, the reaction was carried out with and without the catalyst, light, and H_2O_2 as control experiments. The 50 ppm SA solution, relevant to concentrations measured in wastewater [5], did not show any changes in concentration, as shown in Fig. 1a, when exposed to light without the catalyst and H_2O_2, indicating that SA by itself is not active toward the light. SA combined with H_2O_2 exposed to light without the catalyst showed a 20% reduction in concentration as shown in Fig. 1a, a change that is attributed to the wet oxidation of salicylic acid to products such as quinhydrone as previously reported in the literature [35]. This showed that a catalyst is required for full oxidation of SA since partial oxidation to intermediate organics is undesirable for practical application in wastewater treatment. To investigate the support effect, 500 ppm of undoped MgO was mixed with SA in the dark. The 500 ppm starting point was chosen in agreement with the previous literature values [36]. After 2 h, a 28% reduction in SA concentration was observed, indicating that SA had adsorbed on MgO. The Fe-MgO 500 ppm loading led to 45% adsorption of SA in the dark over 2 h. SA has been previously shown to adsorb on hematite (Fe_2O_3), which can explain the increased adsorption over undoped MgO [37]. Finally, the 500 ppm Fe-MgO loading was tested with 50 ppm SA and 20 mM H_2O_2 in the dark. The 500 ppm catalyst loading and 20 mM H_2O_2 concentration were chosen as the starting point since similar catalysts had been utilized under the same conditions in the literature [38,39]. The kinetics experimental curve followed that for 500 ppm Fe-MgO with no H_2O_2, confirming that light is required for the photo-Fenton-like process to occur. As shown in Fig. 1a, the photo-Fenton-like reaction had significantly faster kinetics and final removal compared to the adsorption process only. Fig. 1b shows the pH change when the 500 ppm loading of the 5% Fe-MgO catalyst was reacted with 50 ppm SA and 20 mM H_2O_2 in the presence of light. The pH of the initial 50 ppm SA solution was 4, and the addition of the catalyst caused a rapid rise to pH 9 within 1 min. The steady-state pH of 11 was reached within 30 min. The pH increase observed here agrees with previously reported pH trends for MgO dissolution, where the MgO surface dissolution results in the release of Mg^{2+} and OH^- and increases the solution pH [28,40]. Importantly, the reactive solution was sampled using AAS at 1 min, 5 min, and 15 min, and no Fe was detected. The rise in pH prevents iron dissolution observed in previous photo-Fenton-like studies that were conducted at lower pH conditions [41,42]. Therefore, the catalytic activity can be attributed to the solid-phase confined iron in Fe-MgO, differently from the homogeneous low pH process [43]. Fig. 1c shows the Mg^{2+} concentration in the solution as a function of time. The final concentration of Mg^{2+} was 66 ppm.

The Fe loading on MgO was varied between 2.5%, 5%, and 10% to find the optimal Fe loading for complete SA degradation. As shown in Fig. 2a, the final conversion for 2.5% Fe-MgO was 93%, with both 5% Fe-MgO and 10% Fe-MgO leading to 100% conversion. Fig. 2b shows that the initial kinetics become faster as the loading is increased from 2.5% to 5% as the rate constant increases from 0.034 min^{-1} to

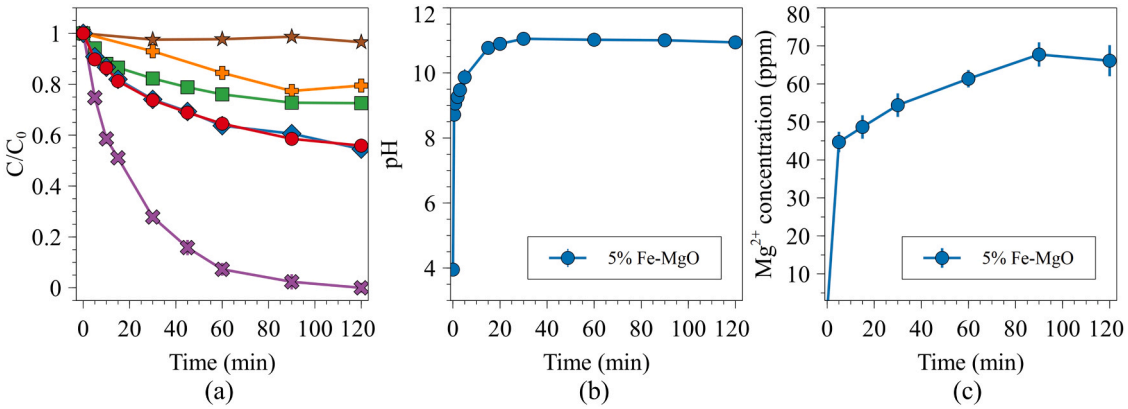

Fig. 1. (a) ★ – 50 ppm SA under light (with no catalyst and no H_2O_2), ✚ - 50 ppm SA + 20 mM H_2O_2 under light (no catalyst), ■ - 500 ppm undoped MgO + 50 pm SA in dark (no H_2O_2), ● – 500 ppm Fe-MgO + 50 ppm SA in dark (no H_2O_2), ◆ - 500 ppm Fe-MgO + 50 ppm SA + 20 mM H_2O_2 in dark, x - 500 ppm Fe-MgO + 50 ppm SA + 20 mM H_2O_2 under light (b) pH variation over time for 500 ppm Fe-MgO during reaction with 50 ppm SA and 20 mM H_2O_2 (c) The Mg^{2+} concentration in the solution for 500 ppm 5% Fe-MgO loading with 50 ppm SA and 20 mM H_2O_2.

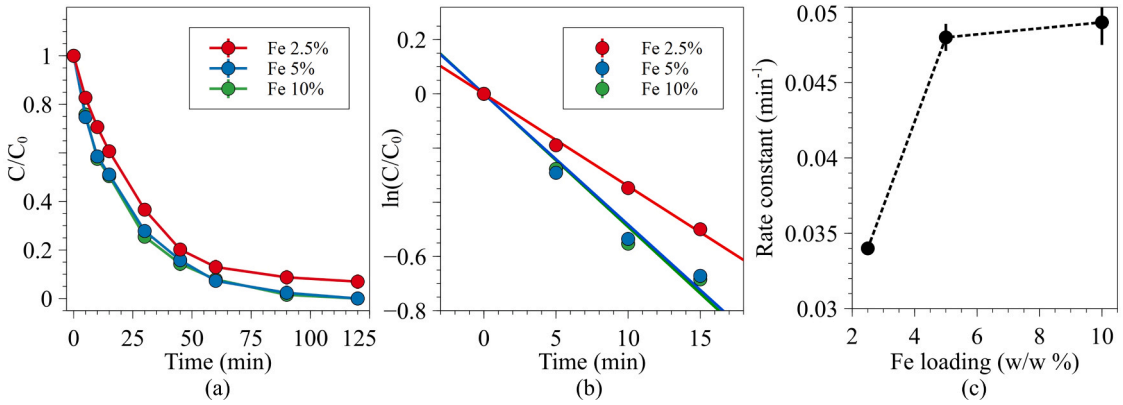

Fig. 2. (a) Relative SA concentration changes as a function of time for each Fe-loading, (b) Initial (0–15 min) kinetics for salicylic acid degradation, (c) First-order rate constant for initial kinetics. (The experiments used 500 ppm of catalyst, 20 mM H_2O_2, and 50 ppm SA).

0.048 min^{-1}, but any improvement in the kinetics and the reaction extent becomes minimal after 5% since doubling the Fe loading after 5% does not lead to a dramatic rise as seen between 2.5% and 5%. The 10% Fe-MgO rate constant is 0.049 min^{-1} and thus, increasing the Fe loading to 10% does not show significant improvement. Fig. 2c illustrates this trend as shown by the rate constant plotted as a function of Fe loading. This demonstrates that 5% is the optimal loading for this reaction.

To find the optimal catalyst loading for SA degradation using the 5% Fe-MgO catalyst 250 ppm, 500 ppm, and 1000 ppm loadings were tested. The initial SA concentration was set to 50 ppm and each experiment utilized a 20 mM H_2O_2 concentration. Increasing the catalyst loading led to an increase in the initial reaction rate and an increase in the final conversion as shown in Fig. 3a. The 500 ppm and 1000 ppm catalyst loadings led to full conversion of SA, while the 250 ppm loading led to a 95% conversion. The 250 ppm, 500 ppm, and 1000 ppm initial rate constants were calculated to be 0.035 min^{-1}, 0.048 min^{-1}, and 0.062 min^{-1}, respectively (Fig. 3b). As shown in Fig. 3c the initial rate constant increased with the increased loading. However, since 500 ppm leads to complete conversion this was selected as the optimal loading. Fig. 3d shows the effect of H_2O_2 concentration on the SA concentration. The 2 mM and 10 mM H_2O_2 concentrations lead to 70% and 85% conversions, respectively. The 20 mM and 30 mM concentrations lead to full conversion of SA. Fig. 3e shows the first-order kinetic fitting for each H_2O_2 concentration. The calculated initial rate constants are shown in Fig. 3f as a function of H_2O_2 concentration. A rise in the initial rate constant was observed for increasing H_2O_2 concentrations, but due to

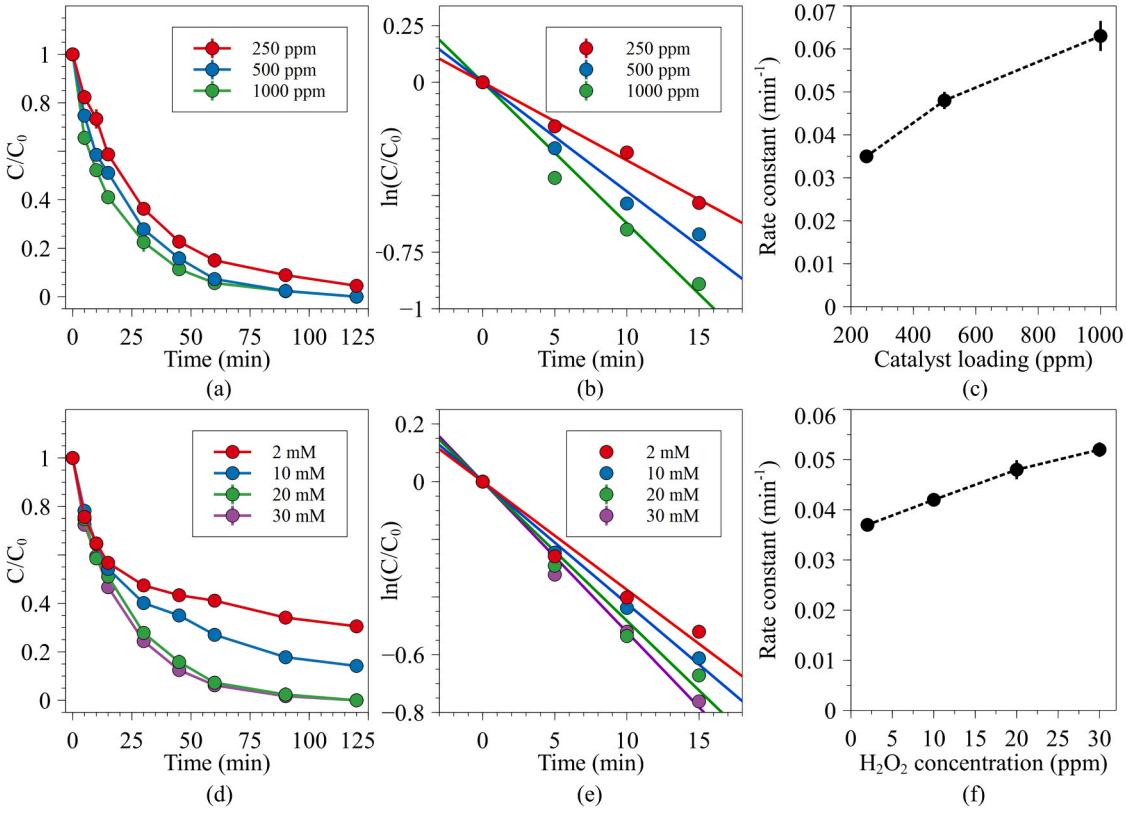

Fig. 3. (a) Relative SA concentration as a function of time for each catalyst loading, (b) first-order kinetic model fits for different catalyst loadings, (c) first-order rate constants (w.r.t. SA) for each catalyst loading, (d) Relative SA concentration as a function of time for each H_2O_2 concentration, (e) first-order model fits for different H_2O_2 concentrations, (f) first-order rate constants (w.r.t. SA) for different H_2O_2 concentrations. (Experiments shown in panels (a)–(c) used 20 mM H_2O_2 and 50 ppm SA. Experiments shown in panels (d)–(f) used 500 ppm catalyst and 50 ppm SA).

full conversion being achieved at 20 mM, this concentration was selected as the optimal.

The 5% Fe-MgO catalyst was used to test stability over several reaction cycles. In each case, 50 ppm SA was used as the starting solution and the optimal 20 mM concentration of H_2O_2 was used. The 5% Fe-MgO catalyst showed stable performance during all 5 cycles as shown in Fig. 4, with a slight decrease in 2-h conversion after the first cycle. The 2-h conversions for each cycle are shown in Table 1 with the initial rate constants. The decrease in the catalytic performance is proposed to be due to surface dissolution and restructuring that leads to active site blocking.

Different reaction time points under the optimal combination of conditions were sampled using time-resolved mass spectrometry. Fig. 5 shows the mass spectra for each time point (0 min, 5 min, 15 min, 30 min, and 120 min). The 0 min mass spectrum shows the SA fragments at *m/z* values of 92.8, 136.9, and 138.3. The salicylic acid was completely degraded by the 120-min time point, suggesting that Fe-MgO can be successfully utilized as a photo-Fenton-like catalyst for cyclic organic compounds.

In order to assess which radicals are critical for the reaction, TBA and $CHCl_3$ were used as radical scavengers. The effect on scavenging molecules on the rate constant are shown in Table 2. The addition of TBA and $CHCl_3$ are intended to investigate the effects of $^{\bullet}OH$ radicals and $^{\bullet}O_2^-$ radicals [22]. The two scavenging molecules yielded similar results for the 50 mM and 100 mM concentrations, indicating that both radicals are active in this reaction. $^{\bullet}OH$ radicals are typically more dominant under acidic and neutral conditions but, shifting the pH to basic conditions allows for other radical species to be responsible for the degradation process as well [44]. As pH increases to basic values the production of $^{\bullet}O_2^-$ becomes favorable, which can explain why both radical scavengers suppress the rate of reaction [23].

3.2. Change in Fe-MgO catalyst bulk crystalline and surface structure and chemical composition

The Fe-MgO catalysts were characterized both as synthesized and post-reaction to study any structural changes that took place due to the reaction. Characterization after one reaction cycle (or multiple) is important in assessing catalyst stability. The Fe-MgO catalyst is active for 5 cycles, albeit with a 7% decrease in overall conversion. To understand the structural changes caused due to the reaction, the bulk crystalline structure and the surface region were first characterized.

Powder X-ray diffraction patterns were collected to confirm the crystal structure of the as-synthesized and post-reaction catalysts. As shown in Fig. 6a, all as-synthesized Fe-MgO catalysts show the pattern for MgO with no extra peaks, indicating that the iron oxide phases exist as small nanoparticles below the detection limit of XRD. The peaks show

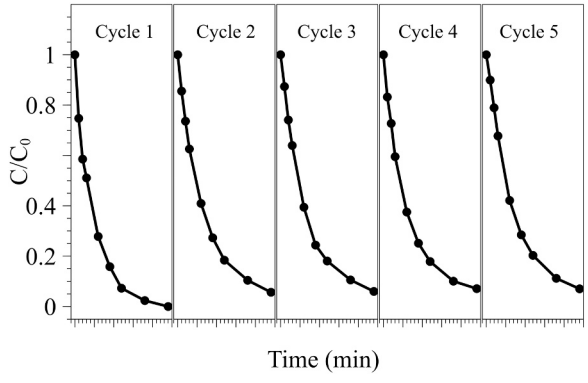

Fig. 4. Performance of 5% Fe-MgO over 5 catalytic cycles. In each case, 50 ppm of SA was reacted with the optimal 20 mM H_2O_2 concentration and 500 ppm catalyst.

Table 1
The initial rate constants for each catalytic cycle for 5% Fe-MgO 500 ppm reacted with 50 ppm SA and 20 mM H_2O_2 (optimal conditions).

Reaction cycle	SA conversion (%)	The initial rate constant (min^{-1})
1	100	0.048
2	94	0.031
3	94	0.030
4	93	0.033
5	93	0.030

broadening after 1 cycle of use as shown in Fig. 6b, with the MgO (3 1 1) and (2 2 2) peaks showing significant broadening and lower intensity. Additionally, all post-reaction catalysts showed a minor peak at 58.9° corresponding to the $Mg(OH)_2$ (1 1 0) plane (JCPDS 00-007-0239) [45]. This indicates that some fraction of the catalyst undergoes dissolution to form hydroxide. All as-synthesized catalysts were dissolved in dilute nitric acid and the solutions were analyzed with AAS to confirm the weight loadings of Fe. The 2.5%, 5%, and 10% catalysts contained 2.5%, 4.9% and 9.5% Fe by weight, respectively. The BET surface areas for as-synthesized 2.5%, 5%, and 10% Fe-MgO were measured using N_2 physisorption to be 170 m^2/g, 171 m^2/g, and 162 m^2/g. The mesoporosity is evident in the isotherms for the post-reaction catalysts as shown in Fig. 6d. Previous work measured the adsorption and showed that mesoporous MgO can lead to faster adsorption kinetics owing to the lower intraparticle diffusion properties when compared to bulk materials [29,46]. Similarly, the use of porous materials for the heterogeneous Fenton reaction has been studied previously using carbon based materials with fast degradation kinetics [15]. The porosity has been shown to facilitate fast reaction kinetics with some of the fastest ever observed for such materials. Hence, the Fe-MgO materials synthesized in this work are expected to exhibit fast transport properties, necessary for fast reaction kinetics.

STEM-EDS imaging was conducted to study the Fe dispersion in the as-synthesized catalysts. Fig. 7a–c show the STEM-EDS maps for each catalyst. The EDS maps display agglomeration of Fe, indicating nanocrystal formation. However, given the lack of iron oxide peaks in XRD, the size of the nanocrystals is expected to be under the detection limit of the XRD measurement. HR-TEM was used to measure the D-spacing for the iron oxide nanocrystals in the as-synthesized catalysts. Fig. 7d–f show the HR-TEM images for each Fe-MgO catalyst with the measured D-spacing. The characteristic D-spacings for hematite (Fe_2O_3) planes (0 2 4), (1 0 4), (1 1 0), (1 1 3), and (2 0 2) were observed [47,48]. This observation confirms that the Fe is present as Fe_2O_3 nanocrystals in the as-synthesized catalyst.

3.3. Fe-MgO NP surface chemical composition characterization

3.3.1. XPS of Fe-MgO NPs

The XPS spectra were acquired to probe the concentration and the chemical state of Fe in the surface region. Fig. 8a–d show the spectra for as-synthesized and post-reaction catalysts. The 2.5% Fe-MgO showed a weak signal in the as-synthesized sample, a 710.8 eV peak corresponding to Fe $2p_{3/2}$ and a weak shoulder centered around 724.9 eV corresponding to Fe $2p_{1/2}$ [49]. The used catalyst showed a weak signal with no discernible peaks. The as-synthesized 5% and 10% Fe-MgO catalysts showed the Fe $2p_{1/2}$ and Fe $2p_{3/2}$ peaks at 724.9 eV and 710.8 eV, respectively. Following 1 catalytic cycle, the peak intensities reduce and show broadening. This effect is significant in the 5% Fe-MgO after 5 cycles of use. The post-reaction 5% Fe-MgO and 10% Fe-MgO catalysts showed new shoulders centered around 709.9 eV and 722.7 eV. The broadening in the post-reaction catalysts can be due to the presence of some minor fraction of Fe^{2+} in addition to the majority of Fe^{3+} sites since the Fe $2p_{1/2}$ peak is centered around 724.0 eV in FeO, while the same peak is reported at 724.1 eV for Fe_2O_3 [49,50]. The shakeup peaks are not well resolved in this sample. The peaks shifting to lower energies is indicative of a reduction in the catalyst [51]. The cyclic

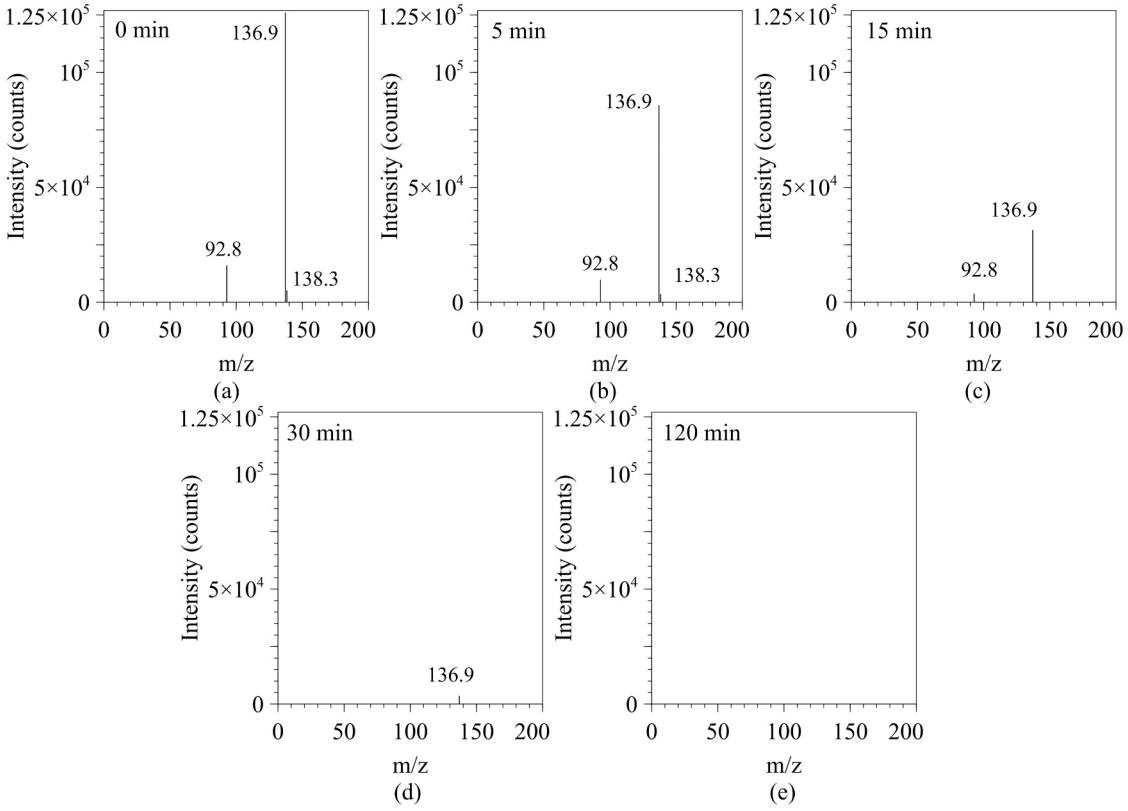

Fig. 5. Time-resolved MS spectra for 5% Fe-MgO reaction with 50 ppm SA and 20 mM H_2O_2.

Table 2
Rate constants for each scavenging treatment.

Quenching treatment	Rate constant k (min^{-1})
No treatment	0.048
50 mM TBA	0.033
100 mM TBA	0.029
50 mM CHCl3	0.033
100 mM CHCl3	0.029

reduction/oxidation of Fe between +3 and +2 during the chain initiation and propagation steps can lead to the presence of Fe^{2+} in the used catalyst [15,23]. Finally Fig. 8d shows the Fe 2p/Mg 2p area ratio, which was used to quantify the Fe concentration in the surface region. The 2.5% Fe-MgO contains approximately 60% less Fe compared to the 5% Fe-MgO, which is consistent with the rate constant trend shown in Fig. 2c. Similarly, 5% Fe-MgO has only 5% less concentration of Fe in the surface region compared to 10% Fe-MgO, which corresponds to the rate constant not changing dramatically between the two samples (Fig. 2c) since the available site concentration on the surface is similar. In the case of 5% Fe-MgO and 10% Fe-MgO, the used samples (after 5 cycles and 1 cycle, respectively) show increased Fe concentrations in the surface region, indicating agglomeration of Fe sites and reduction of Mg due to surface dissolution.

3.4. MgO NP electronic structure characterization

3.4.1. UV–Vis DRS of Fe-MgO NPs

The UV–Vis DR spectra were acquired to elucidate the coordination and oxidation state information of the Fe by studying the LMCT and d-d transfer bands. The LMCT transfer is a key piece of information for photo-Fenton processes since this photoreduction from Fe^{3+} to Fe^{2+} initiates the reaction [17,21,52,53]. Fig. 9 shows the spectra with Kubelka-Munk transformation, where all spectra are normalized by dividing all $F(R_\infty)$ values by the maximum $F(R_\infty)$ value. The Fe_2O_3 bulk hematite spectrum is shown as a reference. As shown in Fig. 9a, the LMCT bands for as-synthesized 2.5%, 5%, and 10% Fe-MgO are centered around 294 nm, 288 nm, and 289 nm, respectively. All three samples show a d-d transition at 480 nm, indicating the presence of iron in the +3 state [54]. The edge energy of the as-synthesized 2.5%, 5%, and 10% Fe-MgO were calculated to be 2.8 eV, 2.79 eV, and 2.79 eV, compared to the reference Fe_2O_3 value of 2.2 eV. Previous XAS analysis confirmed that Fe is in the +3 oxidation state and octahedrally coordinated in as-synthesized catalysts [29]. Fig. 9b shows the UV–vis DR spectra for the post-reaction catalysts. The edge energy of the post-reaction 2.5%, 5%, and 10% Fe-MgO catalysts after one cycle of use was calculated to be 2.75 eV, 2.75 eV, and 2.74 eV, respectively. The reduction of bandgap from the as-synthesized sample values indicates more Fe-O-Fe bridging is present in the post-reaction samples, which indicates agglomeration of Fe sites during the reaction cycle [55]. The 2.5%, 5%, and 10% Fe-MgO catalysts after one cycle of use show LMCT bands around 263 nm. The shift of the LMCT band toward higher energies suggests that the charge-transfer occurs at higher energies, indicating the presence of some tetrahedral Fe^{2+} character in the used samples [56]. The inset in Fig. 9b shows that in addition to the d-d transition at 480 nm, two additional broad low-intensity peaks appear centered around 617 nm and 705 nm. The 617 nm and 705 nm peaks are assigned to d-d transitions in a mixed environment of octahedrally coordinated Fe^{3+} and tetrahedrally coordinated Fe^{2+} sites are present [57, 56,58]. Such mixed coordination Fe centers are present in Fe_3O_4 [59]. This indicates that some Fe^{2+} characteristic is present in the post-reaction sample, which agrees with the Fenton mechanism of alternating between +2 and +3 oxidation states.

4. Importance of MgO surface dissolution and bifunctionality

SA has been studied in the homogeneous Fenton literature, with a report showing the limitations of the homogenous process due to the

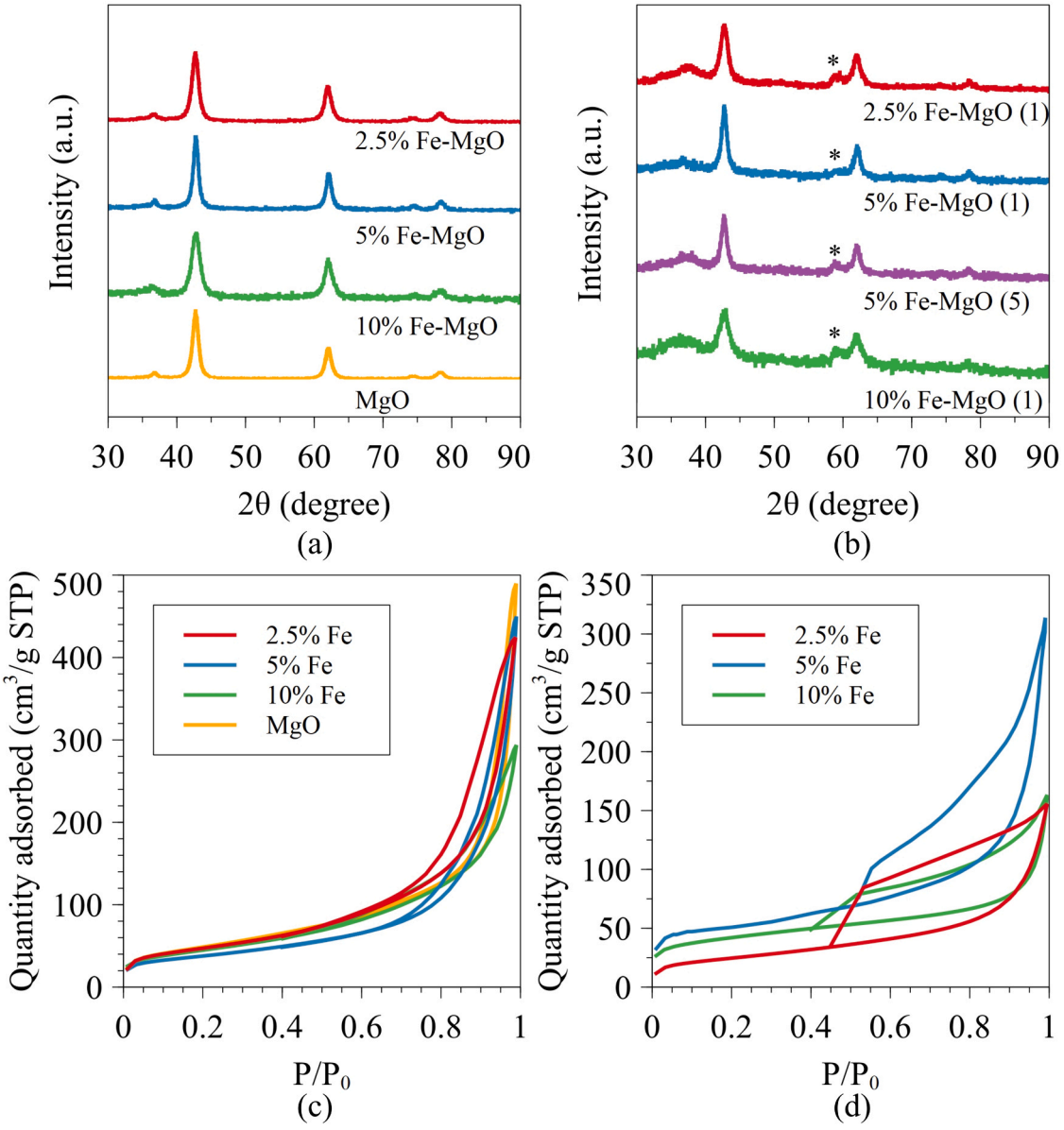

Fig. 6. (a) XRD patterns for as-synthesized Fe-MgO catalysts and MgO, (b) XRD patterns for post-reaction Fe-MgO catalysts used for 1 cycle (denoted by (1)) and 5% Fe-MgO used for 5 cycles (denoted by (5)), (c) N_2 physisorption isotherms for as-synthesized Fe-MgO catalysts and MgO, (d) N_2 physisorption isotherms for post-reaction Fe-MgO catalysts.

reaction termination caused by stable complex formation between SA and $Fe^{3+}_{(aq)}$ [60]. In contrast, the heterogeneous degradation of SA has been reported using a strongly acidic ion-exchange resin (SAIER) with Fe^{3+} bound by sulfonic groups as a photo-Fenton-like catalyst, SA can be completely mineralized via the photo-Fenton-like process in an aqueous solution [43]. Therefore, the heterogeneous reaction is more suitable for this molecule due to the ability to achieve complete mineralization by avoiding strong complexation with Fe^{3+}. However, this study shows that both dissolved iron and solid-phase iron participate in the reaction at pH 3 [43]. Similarly, bulk Fe-based catalysts such as goethite and magnetite reported in the literature leach Fe into the solution in varying amounts in the pH range of 3–9 [42,61,62]. In the Fe-MgO catalyst reported herein, the MgO support undergoes surface dissolution and renders the solution basic (pH ~ 10–11), allowing for the heterogeneous reaction to dominate [28]. Fig. 10 depicts this bifunctional catalyst operation, with a proposed ROS generation pathway based on findings from the quenching experiments. The pH self-adjustment ensures that no Fe is leached into the aqueous phase, which eliminates the need for any downstream Fe removal treatment. This advantage offered by the bifunctional Fe-MgO can be a novel strategy to treat recalcitrant organic contaminants in wastewater without further addition of $Fe^{2+}/Fe^{3+}_{(aq)}$ to the effluent.

5. Conclusions

In summary, a novel Fe-MgO catalyst was demonstrated to be an effective bifunctional catalyst for the photo-degradation of recalcitrant organic contaminants. The catalyst was able to serve the two functions: providing the active site for ROS generation and adjusting the solution pH, both of which have been demonstrated to be a highly effective strategies for degrading organics in wastewater without leaching Fe^{3+}/Fe^{2+} into the solution. SA was successfully degraded under the optimal conditions of 50 ppm SA, 20 mM H_2O_2, and 500 ppm 5% Fe-MgO over a 2 h reaction time. The reusability of the catalyst was assessed by recycling five times with minimal loss in activity. Characterization of the post-reaction catalyst via XPS and UV–Vis indicated the presence of Fe^{2+}

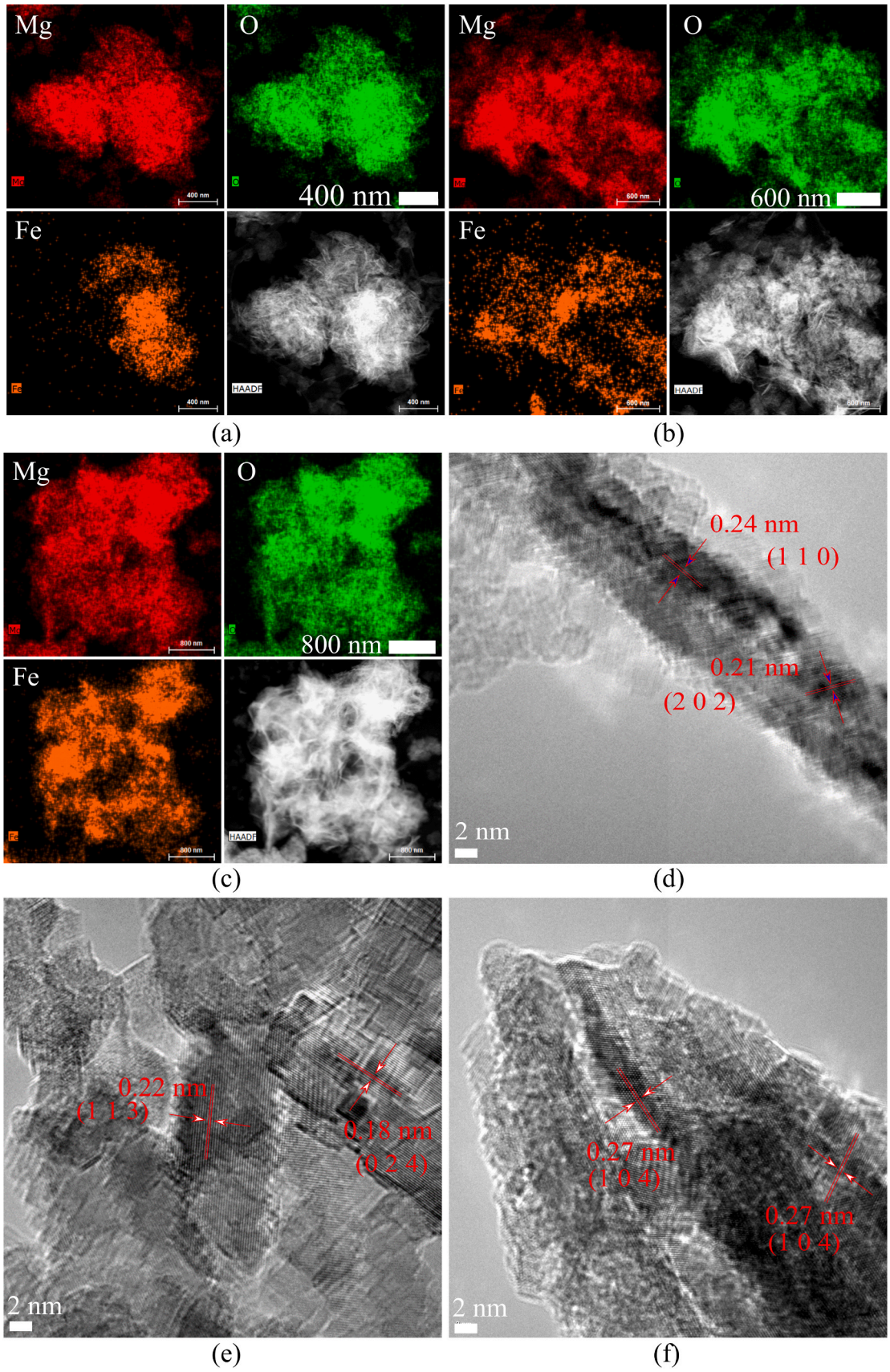

Fig. 7. STEM-EDS maps for (a) 2.5% Fe-MgO, (b) 5% Fe-MgO, (c) 10% Fe-MgO catalysts. HR-TEM images for (d) 2.5% Fe-MgO, (e) 5% Fe-MgO, (f) 10% Fe-MgO catalysts.

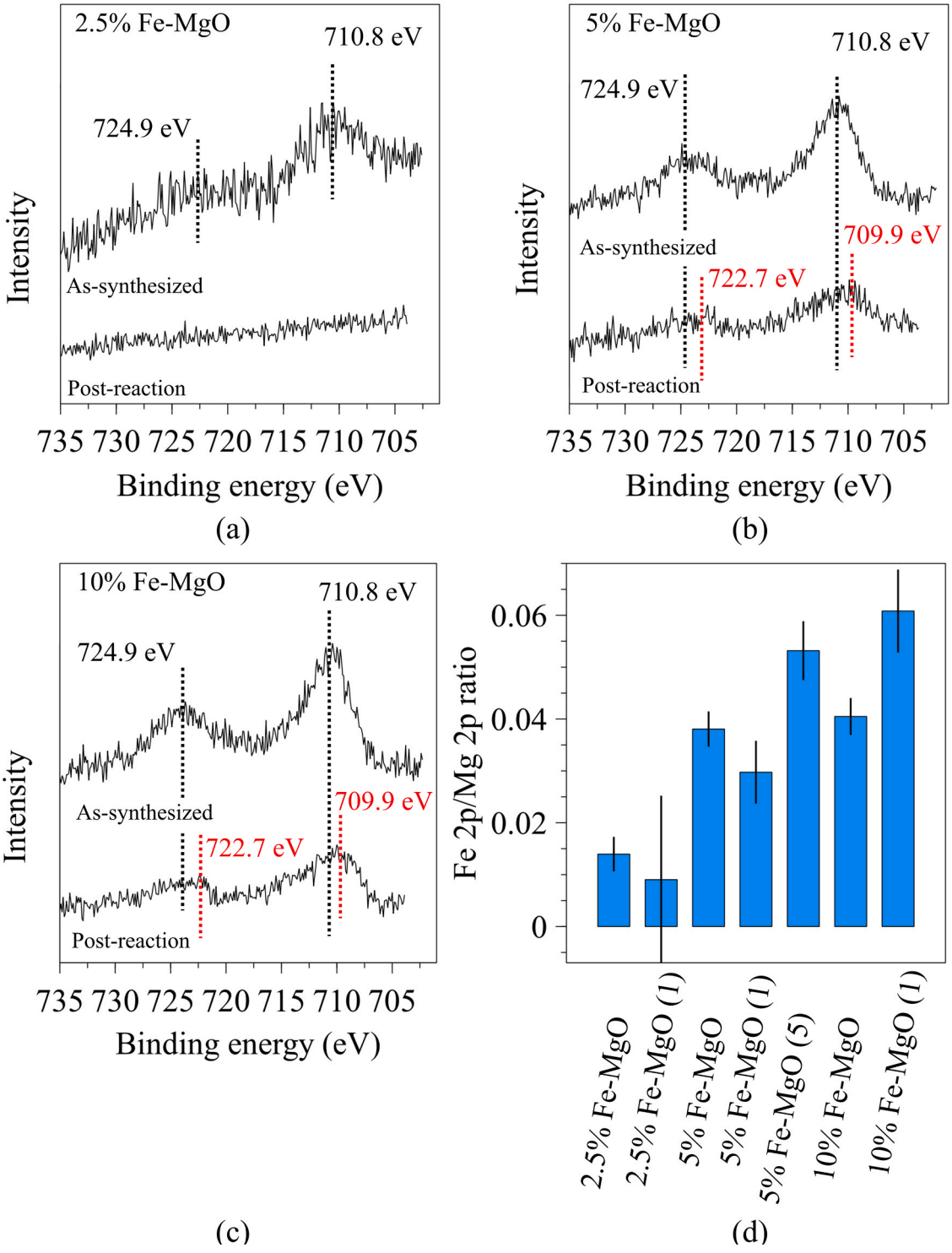

Fig. 8. XPS spectra for as-synthesized and post-reaction catalysts (a) 2.5% Fe-MgO, (b) 5% Fe-MgO, (c) 10% Fe-MgO, (d) Fe 2p/Mg 2p peak area ratio with error bars shown.

due to the redox cycle of the active site during ROS production. Furthermore, the complete mineralization of SA to H_2O and CO_2 shows that this catalyst has potential for further studies with more complex wastewater compositions and other target molecules. Therefore, bifunctional photo-Fenton-like catalysts utilizing basic supports are a class of catalysts that require more work in terms of target contaminant molecules and process optimization.

CRediT authorship contribution statement

M.S.: Conceptualization. **M.S., A.K., L.Z., J.B.**: Investigation. **M.S.**: Visualization. **M.S., J.B.**: Writing - original draft. **M.S., J.B.**: Writing - review & editing. **C.W., L.Z., J.B.**: Resources. **J.B.**: Supervision. **J.B.**: Funding acquisition.

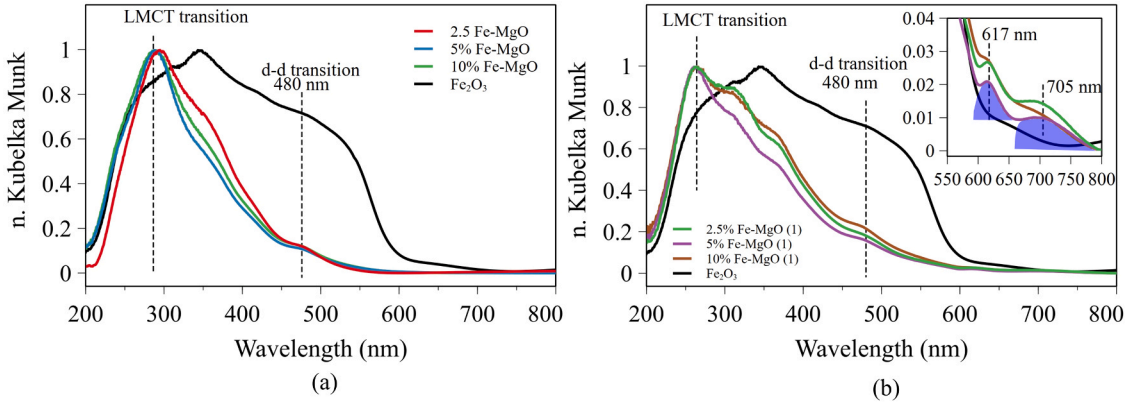

Fig. 9. Normalized Kebulka-Munk transformed UV–vis diffuse reflectance spectra for (a) as-synthesized Fe-MgO catalysts, (b) post-reaction Fe-MgO catalysts.

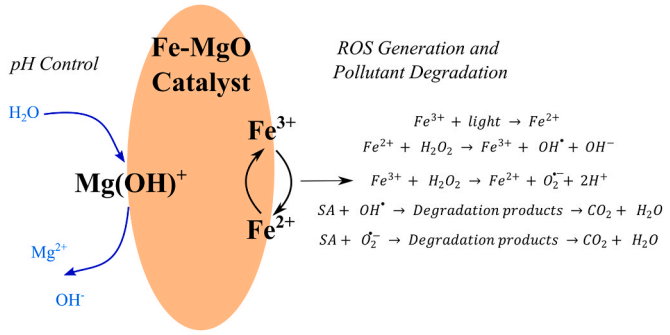

Fig. 10. The proposed ROS generation and SA degradation pathway and the MgO surface dissolution enabling pH control.

Declaration of Competing Interest

The authors declare that they have no known competing financial interests or personal relationships that could have appeared to influence the work reported in this paper.

Acknowledgments

This material is based upon work supported by the National Science Foundation under Grant No. CHE 1710120. HRTEM and STEM-EDS was carried out on JEOL2100F and FEI Talos 200X at the Center for Functional Nanomaterials, Brookhaven National Laboratory, which is supported by the US Department of Energy, Office of Basic Energy Sciences, under Contract No. DE-SC0012704. The authors acknowledge Prof. Mark Snyder and Mr. Lohit Sharma for assistance with obtaining BET data, Prof. Israel Wachs and Mr. Daniyal Kiani for assistance with obtaining UV-Vis-DRS data, and Prof. Steven McIntosh and Mr. John Sakizadeh for assistance in obtaining UV-Vis data.

References

[1] Environmental Engineering for the 21st Century, National Academies Press, Washington, D.C., 2019. https://doi.org/10.17226/25121.
[2] M.A. Montgomery, M. Elimelech, Water and sanitation in developing countries: including health in the equation - millions suffer from preventable illnesses and die every year, Environ. Sci. Technol. 41 (2007) 17–24, https://doi.org/10.1021/es072435t.
[3] M.A. Shannon, P.W. Bohn, M. Elimelech, J.G. Georgiadis, B.J. Marīas, A.M. Mayes, Science and technology for water purification in the coming decades, Nature 452 (2008) 301–310, https://doi.org/10.1038/nature06599.
[4] M. Silva, J. Baltrusaitis, A review of phosphate adsorption on Mg-containing materials: kinetics, equilibrium, and mechanistic insights, Environ. Sci. Water Res. Technol. 6 (2020) 3178–3194, https://doi.org/10.1039/D0EW00679C.
[5] N.H. Tran, M. Reinhard, K.Y.H. Gin, Occurrence and fate of emerging contaminants in municipal wastewater treatment plants from different geographical regions-a review, Water Res. 133 (2018) 182–207, https://doi.org/10.1016/j.watres.2017.12.029.
[6] P. Verlicchi, E. Zambello, Pharmaceuticals and personal care products in untreated and treated sewage sludge: occurrence and environmental risk in the case of application on soil - a critical review, Sci. Total Environ. 538 (2015) 750–767, https://doi.org/10.1016/j.scitotenv.2015.08.108.
[7] J. Rivera-Utrilla, M. Sánchez-Polo, M.Á. Ferro-García, G. Prados-Joya, R. Ocampo-Pérez, Pharmaceuticals as emerging contaminants and their removal from water. A review, Chemosphere 93 (2013) 1268–1287, https://doi.org/10.1016/j.chemosphere.2013.07.059.
[8] M. Patel, R. Kumar, K. Kishor, T. Mlsna, C.U. Pittman, D. Mohan, Pharmaceuticals of emerging concern in aquatic systems: chemistry, occurrence, effects, and removal methods, Chem. Rev. 119 (2019) 3510–3673, https://doi.org/10.1021/acs.chemrev.8b00299.
[9] M.L. Sikosana, K. Sikhwivhilu, R. Moutloali, D.M. Madyira, Municipal wastewater treatment technologies: a review, Procedia Manuf. (2019) 1018–1024, https://doi.org/10.1016/j.promfg.2019.06.051.
[10] B.E. Cowie, V. Porley, N. Robertson, Solar disinfection (SODIS) provides a much underexploited opportunity for researchers in Photocatalytic Water Treatment (PWT), ACS Catal. 10 (2020) 11779–11782, https://doi.org/10.1021/acscatal.0c03325.
[11] B.M. Souza, B.S. Souza, T.M. Guimarães, T.F.S. Ribeiro, A.C. Cerqueira, G. L. Sant'Anna, M. Dezotti, Removal of recalcitrant organic matter content in wastewater by means of AOPs aiming industrial water reuse, Environ. Sci. Pollut. Res. 23 (2016) 22947–22956, https://doi.org/10.1007/s11356-016-7476-5.
[12] S. Dong, M.A. Page, N. Massalha, A. Hur, K. Hur, K. Bokenkamp, E.D. Wagner, M. J. Plewa, Toxicological comparison of water, wastewaters, and processed wastewaters, Environ. Sci. Technol. 53 (2019) 9139–9147, https://doi.org/10.1021/acs.est.9b00827.
[13] M. Silva, J. Baltrusaitis, Destruction of emerging organophosphate contaminants in wastewater using the heterogeneous iron-based photo-Fenton-like process, J. Hazard. Mater. Lett. 2 (2021), 100012, https://doi.org/10.1016/j.hazl.2020.100012.
[14] D.M. Golea, A. Upton, P. Jarvis, G. Moore, S. Sutherland, S.A. Parsons, S.J. Judd, THM and HAA formation from NOM in raw and treated surface waters, Water Res. 112 (2017) 226–235, https://doi.org/10.1016/j.watres.2017.01.051.
[15] Y. Zhu, R. Zhu, Y. Xi, J. Zhu, G. Zhu, H. He, Strategies for enhancing the heterogeneous fenton catalytic reactivity: a review, Appl. Catal. B Environ. 255 (2019), 117739, https://doi.org/10.1016/j.apcatb.2019.05.041.
[16] S. Wang, A comparative study of Fenton and Fenton-like reaction kinetics in decolourisation of wastewater, Dyes Pigment. 76 (2008) 714–720, https://doi.org/10.1016/j.dyepig.2007.01.012.
[17] S. Giannakis, A review of the concepts, recent advances and niche applications of the (photo) Fenton process, beyond water/wastewater treatment: surface functionalization, biomass treatment, combatting cancer and other medical uses, Appl. Catal. B Environ. 248 (2019) 309–319, https://doi.org/10.1016/j.apcatb.2019.02.025.
[18] G. Boczkaj, A. Fernandes, Wastewater treatment by means of advanced oxidation processes at basic pH conditions: a review, Chem. Eng. J. 320 (2017) 608–633, https://doi.org/10.1016/j.cej.2017.03.084.
[19] M.C. Pereira, L.C.A. Oliveira, E. Murad, Iron oxide catalysts: Fenton and Fentonlike reactions – a review, Clay Miner. 47 (2012) 285–302, https://doi.org/10.1180/claymin.2012.047.3.01.
[20] C. di Luca, P. Massa, R. Fenoglio, F.M. Cabello, Improved Fe $_2$ O $_3$ /Al $_2$ O $_3$ as heterogeneous Fenton catalysts for the oxidation of phenol solutions in a continuous reactor, J. Chem. Technol. Biotechnol. 89 (2014) 1121–1128, https://doi.org/10.1002/jctb.4412.
[21] J. Herney-Ramirez, M.A. Vicente, L.M. Madeira, Heterogeneous photo-Fenton oxidation with pillared clay-based catalysts for wastewater treatment: a review, Appl. Catal. B Environ. 98 (2010) 10–26, https://doi.org/10.1016/j.apcatb.2010.05.004.
[22] S. Guo, W. Yang, L. You, J. Li, J. Chen, K. Zhou, Simultaneous reduction of Cr(VI) and degradation of tetracycline hydrochloride by a novel iron-modified rectorite

composite through heterogeneous photo-Fenton processes, Chem. Eng. J. 393 (2020), 124758, https://doi.org/10.1016/j.cej.2020.124758.
[23] A.V. Vorontsov, Advancing Fenton and photo-Fenton water treatment through the catalyst design, J. Hazard. Mater. 372 (2019) 103–112, https://doi.org/10.1016/j.jhazmat.2018.04.033.
[24] J.F. Barona, D.F. Morales, L.F. González-Bahamón, C. Pulgarín, L.N. Benítez, Shift from heterogeneous to homogeneous catalysis during resorcinol degradation using the solar photo-Fenton process initiated at circumneutral pH, Appl. Catal. B Environ. 165 (2015) 620–627, https://doi.org/10.1016/j.apcatb.2014.10.053.
[25] F. Martínez, G. Calleja, J.A. Melero, R. Molina, Heterogeneous photo-Fenton degradation of phenolic aqueous solutions over iron-containing SBA-15 catalyst, Appl. Catal. B Environ. 60 (2005) 181–190, https://doi.org/10.1016/j.apcatb.2005.03.004.
[26] M. Fang, R. Zheng, Y. Wu, D. Yue, X. Qian, Y. Zhao, Z. Bian, CuO nanosheet as a recyclable Fenton-like catalyst prepared from simulated Cu(ii) waste effluents by alkaline H 2 O 2 reaction, Environ. Sci. Nano 6 (2019) 105–114, https://doi.org/10.1039/c8en00930a.
[27] X. Zhang, Y. Zhang, Z. Yu, X. Wei, W.D. Wu, X. Wang, Z. Wu, Synergistic activation of peroxymonosulfate via in situ growth FeCo2O4 nanoparticles on natural rectorite: role of transition metal ions and hydroxyl groups, Chemosphere 263 (2021), 127965, https://doi.org/10.1016/j.apcatb.2019.118335.
[28] P. Stolzenburg, A. Capdevielle, S. Teychené, B. Biscans, Struvite precipitation with MgO as a precursor: application to wastewater treatment, Chem. Eng. Sci. 133 (2014) 9–15, https://doi.org/10.1016/j.ces.2015.03.008.
[29] M. Silva, V. Murzin, L. Zhang, J.P. Baltrus, J. Baltrusaitis, Transition metal doped MgO nanoparticles for nutrient recycling: an alternate Mg source for struvite synthesis from wastewater, Environ. Sci. Nano 7 (2020) 3482–3496, https://doi.org/10.1039/d0en00660b.
[30] S.W. Bian, J. Baltrusaitis, P. Galhotra, V.H. Grassian, A template-free, thermal decomposition method to synthesize mesoporous MgO with a nanocrystalline framework and its application in carbon dioxide adsorption, J. Mater. Chem. 20 (2010) 8705–8710, https://doi.org/10.1039/c0jm01261k.
[31] E.I. Ross-medgaarden, I.E. Wachs, Structural determination of bulk and surface tungsten oxides with UV–vis diffuse reflectance spectroscopy and raman spectroscopy, J. Phys. Chem. C 111 (2007) 15089–15099, https://doi.org/10.1021/jp074219c.
[32] P. Kebulka, F. Munk, Ein Beitrag Zur Optik Der Farbanstriche, Z. Tech. Phys. 12 (1931) 593–601.
[33] E. Wicke, Spectroscopy in Heterogeneous Catalysis. Von W. N. Delgass, G. L. Haller, R. Kellerman and J. H. Lunsford. Academic Press, New York 1979. X, 341 S., 117 Abb., geb. $ 35.00, Angew. Chem. 94 (1982) 324–325, https://doi.org/10.1002/ange.19820940446.
[34] Q. Li, G. Wei, Y. Yang, Z. Li, L. Zhang, L. Shao, S. Lai, Insight into the enhanced catalytic activity of a red mud based Fe 2 O 3 /Zn–Al layered double hydroxide in the photo-Fenton reaction, Catal. Sci. Technol. (2020), https://doi.org/10.1039/d0cy01539c.
[35] S. Collado, L. Garrido, A. Laca, M. Diaz, Wet oxidation of salicylic acid solutions, Environ. Sci. Technol. 44 (2010) 8629–8635, https://doi.org/10.1021/es1021944.
[36] M.B. Kasiri, H. Aleboyeh, A. Aleboyeh, Degradation of Acid Blue 74 using Fe-ZSM5 zeolite as a heterogeneous photo-Fenton catalyst, Appl. Catal. B Environ. 84 (2008) 9–15, https://doi.org/10.1016/j.apcatb.2008.02.024.
[37] D. Kovačević, N. Kallay, I. Antol, A. Pohlmeier, H. Lewandowski, H.D. Narres, The use of electrokinetic potential in the interpretation of adsorption phenomena: adsorption of salicylic acid on hematite, Colloids Surf. A Physicochem. Eng. Asp. (1998) 261–267, https://doi.org/10.1016/S0927-7757(97)00283-5.
[38] M. Bayat, M. Sohrabi, S.J. Royaee, Degradation of phenol by heterogeneous Fenton reaction using Fe/clinoptilolite, J. Ind. Eng. Chem. 18 (2012) 957–962, https://doi.org/10.1016/j.jiec.2011.09.004.
[39] J. Zhang, X. Zhang, Y. Wang, Degradation of phenol by a heterogeneous photo-Fenton process using Fe/Cu/Al catalysts, RSC Adv. 6 (2016) 13168–13176, https://doi.org/10.1039/c5ra20897a.
[40] V.S. Birchal, S.D.F. Rocha, M.B. Mansur, V.S.T. Ciminelli, A simplified mechanistic analysis of the hydration of magnesia, Can. J. Chem. Eng. 79 (2001) 507–511, https://doi.org/10.1002/cjce.5450790406.
[41] Z. Zhang, Z. Ouyang, J. Yang, Y. Liu, C. Yang, Z. Dang, High mineral adsorption of glyphosate versus diethyl phthalate and tetracycline, during visible light photodegradation with goethite and oxalate, Environ. Chem. Lett. 17 (2019) 1421–1428, https://doi.org/10.1007/s10311-019-00877-x.
[42] Y. Yang, Q. Deng, W. Yan, C. Jing, Y. Zhang, Comparative study of glyphosate removal on goethite and magnetite: adsorption and photo-degradation, Chem. Eng. J. 352 (2018) 581–589, https://doi.org/10.1016/j.cej.2018.07.058.
[43] J. Feng, X. Hu, P.L. Yue, Degradation of salicylic acid by photo-assisted Fenton reaction using Fe ions on strongly acidic ion exchange resin as catalyst, Chem. Eng. J. 100 (2004) 159–165, https://doi.org/10.1016/j.cej.2004.01.031.
[44] H. Lee, H.J. Lee, D.L. Sedlak, C. Lee, pHDependent reactivity of oxidants formed by iron and copper-catalyzed decomposition of hydrogen peroxide, Chemosphere 92 (2013) 652–658, https://doi.org/10.1016/j.chemosphere.2013.01.073.
[45] C. Liu, R. Zhang, K. Shen, T. Liu, W. Wen, D. Wang, An in situ kinetic study of the dehydration of brucite using synchrotron X-ray powder diffraction, Can. Mineral. 56 (2018) 101–108, https://doi.org/10.3749/canmin.1700052.
[46] J. Zhou, S. Yang, J. Yu, Facile fabrication of mesoporous MgO microspheres and their enhanced adsorption performance for phosphate from aqueous solutions, Colloids Surf. A Physicochem. Eng. Asp. 379 (2011) 102–108, https://doi.org/10.1016/j.colsurfa.2010.11.050.
[47] R. dos Santos, M. Patel, J. Cuadros, Z. Martins, Influence of mineralogy on the preservation of amino acids under simulated Mars conditions, Icarus 277 (2016) 342–353, https://doi.org/10.1016/j.icarus.2016.05.029.
[48] R.L. Blake, R.E. Hessevick, T. Zoltai, L.W. Finger, Refinement of the hematite structure, Am. Mineral. 51 (1966) 123–129.
[49] A.N. Mansour, R.A. Brizzolara, Characterization of the surface of γ-Fe2O3 powder by XPS, Surf. Sci. Spectra 4 (1996) 351–356, https://doi.org/10.1116/1.1247832.
[50] A.N. Mansour, R.A. Brizzolara, Characterization of the surface of FeO Powder by XPS, Surf. Sci. Spectra 4 (1996) 345–350, https://doi.org/10.1116/1.1247831.
[51] L. Nguyen, F.F. Tao, Y. Tang, J. Dou, X.J. Bao, Understanding catalyst surfaces during catalysis through near ambient pressure X-ray photoelectron spectroscopy, Chem. Rev. 119 (2019) 6822–6905, https://doi.org/10.1021/acs.chemrev.8b00114.
[52] J.J. Pignatello, E. Oliveros, A. MacKay, Advanced oxidation processes for organic contaminant destruction based on the fenton reaction and related chemistry, Crit. Rev. Environ. Sci. Technol. 36 (2006) 1–84, https://doi.org/10.1080/10643380500326564.
[53] C. Ruales-Lonfat, J.F. Barona, A. Sienkiewicz, M. Bensimon, J. Vélez-Colmenares, N. Benítez, C. Pulgarín, Iron oxides semiconductors are efficients for solar water disinfection: a comparison with photo-Fenton processes at neutral pH, Appl. Catal. B Environ. 166–167 (2015) 497–508, https://doi.org/10.1016/j.apcatb.2014.12.007.
[54] A.C. Scheinost, A. Chavernas, V. Barrón, J. Torrent, Use and limitations of second-derivative diffuse reflectance spectroscopy in the visible to near-infrared range to identify and quantify Fe oxide minerals in soils, Clays Clay Miner. 46 (1998) 528–536, https://doi.org/10.1346/CCMN.1998.0460506.
[55] A. Chakrabarti, I.E. Wachs, Molecular structure–reactivity relationships for olefin metathesis by Al 2 O 3 -supported surface MoO x sites, ACS Catal. 8 (2018) 949–959, https://doi.org/10.1021/acscatal.7b03598.
[56] G.B. Kauffman, Inorganic Chemistry, 2nd Edition (Miessler, Gary L.; Tarr, Donald A.), J. Chem. Educ. 77 (2000) 165, https://doi.org/10.1021/ed077p165.1.
[57] L.I. Granone, A.C. Ulpe, L. Robben, S. Klimke, M. Jahns, F. Renz, T.M. Gesing, T. Bredow, R. Dillert, D.W. Bahnemann, Effect of the degree of inversion on optical properties of spinel ZnFe2O4, Phys. Chem. Chem. Phys. 20 (2018) 28267–28278, https://doi.org/10.1039/c8cp05061a.
[58] D.M. Sherman, Electronic structures of iron oxides and silicates, in: Advanced Mineralogy, Springer Berlin Heidelberg, 1994, pp. 327–340, https://doi.org/10.1007/978-3-642-78523-8_22.
[59] J. Noh, O.I. Osman, S.G. Aziz, P. Winget, J.L. Brédas, Magnetite Fe3O4 (111) surfaces: impact of defects on structure, stability, and electronic properties, Chem. Mater. 27 (2015) 5856–5867, https://doi.org/10.1021/acs.chemmater.5b02885.
[60] A. Goi, Y. Veressinina, M. Trapido, Degradation of salicylic acid by Fenton and modified Fenton treatment, Chem. Eng. J. 143 (2008) 1–9, https://doi.org/10.1016/j.cej.2008.01.018.
[61] M.C. Lu, Oxidation of chlorophenols with hydrogen peroxide in the presence of goethite, Chemosphere 40 (2000) 125–130, https://doi.org/10.1016/S0045-6535(99)00213-1.
[62] M.C. Lu, J.N. Chen, H.H. Huang, Role of goethite dissolution in the oxidation of 2-chlorophenol with hydrogen peroxide, Chemosphere 46 (2002) 131–136, https://doi.org/10.1016/S0045-6535(01)00076-5.